







Ferrimagnetic coupling between cobalt and light rare-earth samarium induced by dense hydrogenation of SmCo_5 permanent magnet under high pressures

Naoki Ishimatsu ^{1,*}, Kentaro Ishimoto,¹ Kouji Sakaki ², Yumiko Nakamura ², Naomi Kawamura ³, Saori I. Kawaguchi,³ Naohisa Hirao ³ and Satoshi Nakano ⁴

¹Graduate School of Advanced Science and Engineering, Hiroshima University 1-3-1 Kagamiyama, Higashihiroshima, Hiroshima 739-8526, Japan

²National Institute of Advanced Industrial Science and Technology, AIST Tsukuba West, 16-1 Onogawa, Tsukuba, Ibaraki, 305-8569, Japan

³Japan Synchrotron Radiation Research Institute (JASRI), 1-1-1 Sayo, Hyogo 679-5198, Japan

⁴National Institute for Materials Science (NIMS), 1-1 Namiki, Tsukuba, Ibaraki 305-0044, Japan



(Received 9 November 2022; revised 3 January 2023; accepted 18 January 2023; published 3 February 2023)

X-ray magnetic circular dichroism, x-ray powder diffraction and first-principles calculations revealed that dense hydrogenation of a Gd-doped SmCo_5H_x compound ($\text{Sm}_{0.92}\text{Gd}_{0.08}\text{Co}_5\text{H}_x$), ranging up to $x \approx 13.5$, flips the direction of Sm $4f$ magnetic moments. Consequently, the magnetic coupling of Sm $4f$ with Co $3d$ moments changes to ferrimagnetic from the conventional ferromagnetic coupling. The ferrimagnetic structure possessed significantly lower Curie temperatures of $T_C \leq 131$ K, which is in contrast to the extremely high $T_C \sim 1300$ K of a SmCo_5 permanent magnet. Structural parameters of two hydrogenation-induced crystal structures were determined carefully by x-ray powder diffraction. Large volume expansion exceeding $V/V_0 = 1.3$ indicates that hydrogen occupation in the Sm-3Co tetrahedron occurred above 1 GPa. The hydrogen in the tetrahedron dominates the ferromagnetic coupling between the interatomic Co $3d$ –Sm $5d$ electron orbitals, which plays an important role in the induction of the ferrimagnetic structure of SmCo_5H_x .

DOI: [10.1103/PhysRevMaterials.7.024401](https://doi.org/10.1103/PhysRevMaterials.7.024401)

I. INTRODUCTION

Magnetism in compounds of $4f$ rare-earth (RE) metals with $3d$ transition metals (TM) is characterized by different magnetic coupling depending on the number of $4f$ electrons, n_{4f} . The magnetic moment of $4f$ electrons in light RE atoms ($n_{4f} \leq 6$) is ferromagnetically coupled with the magnetic moments of TM = Co or Fe, whereas the moment of heavy RE elements ($n_{4f} \geq 7$) is ferrimagnetically coupled. These magnetic couplings originate from Hund's third rule, intra-atomic RE $4f$ –RE $5d$ exchange interaction, and interatomic RE $5d$ –TM $3d$ exchange interaction [1–3]. The intra-atomic RE $4f$ –RE $5d$ ferromagnetic and interatomic RE $5d$ –TM $3d$ antiferromagnetic exchanges work along the same direction in compounds with both light and heavy RE elements. In contrast, the spin-orbit coupling of RE $4f$ electrons is governed by Hund's third rule, which orients the $4f$ spin and orbital moments in the opposite or same direction depending on n_{4f} : $4f$ orbital moment aligns antiparallel and parallel to $4f$ spin moment for the light and heavy RE elements, respectively. Light RE metals typically have a larger $4f$ orbital moment than their $4f$ spin moment; therefore, the dominant RE $4f$ orbital moment aligns parallel to the TM spin moment, and the RE $4f$ spin moment aligns antiparallel. In contrast both $4f$ orbital and spin magnetic moments for heavy RE metals are oriented antiparallel to the TM spin moment. This charac-

teristic magnetic coupling is fulfilled not only in crystalline magnetic compounds but also in glasslike alloys [4,5] and RE-TM interfaces in magnetic thin films [6].

Hydrogenation at moderate pressures below 1 GPa induces modification of Curie temperature, magnetization, and magnetic anisotropy [7], whereas the hydrogenation process under high pressures above 1 GPa leads to a drastic change in the magnetic coupling. Mitsui *et al.* recently discovered that hydrogenation in an H_2 atmosphere at more than 12 GPa reverses the magnetic structure of Laves phase GdFe_2 from the conventional ferrimagnetic coupling to a ferromagnetic one [8,9]. Flipping of Fe moment to the parallel direction of the net magnetization from antiparallel was observed by Mössbauer spectroscopy with circularly polarized γ rays. X-ray magnetic circular dichroism (XMCD) spectra at the Gd $L_{2,3}$ edges indicated that the direction of Gd moment remains parallel to the external magnetic field H_{ext} after hydrogenation. Therefore, the ferrimagnetic coupling working between Fe and heavy rare-earth Gd atoms is ruled out of the allowed magnetic coupling post hydrogenation, and a ferromagnetic coupling emerges subsequent to the paramagnetic phase at pressures of 3–12 GPa.

It is of interest to examine whether the same hydrogenation effect for the magnetic coupling occurs in RE-TM compounds not only with heavy rare-earth elements but also with light rare-earth elements, which is crucial to interpret the mechanism of flipping the magnetic coupling between RE and TM atoms. In this paper, we studied hydrogenation effects on the magnetic states in a light rare-earth samarium compound:

*ishimatsunaoki@hiroshima-u.ac.jp

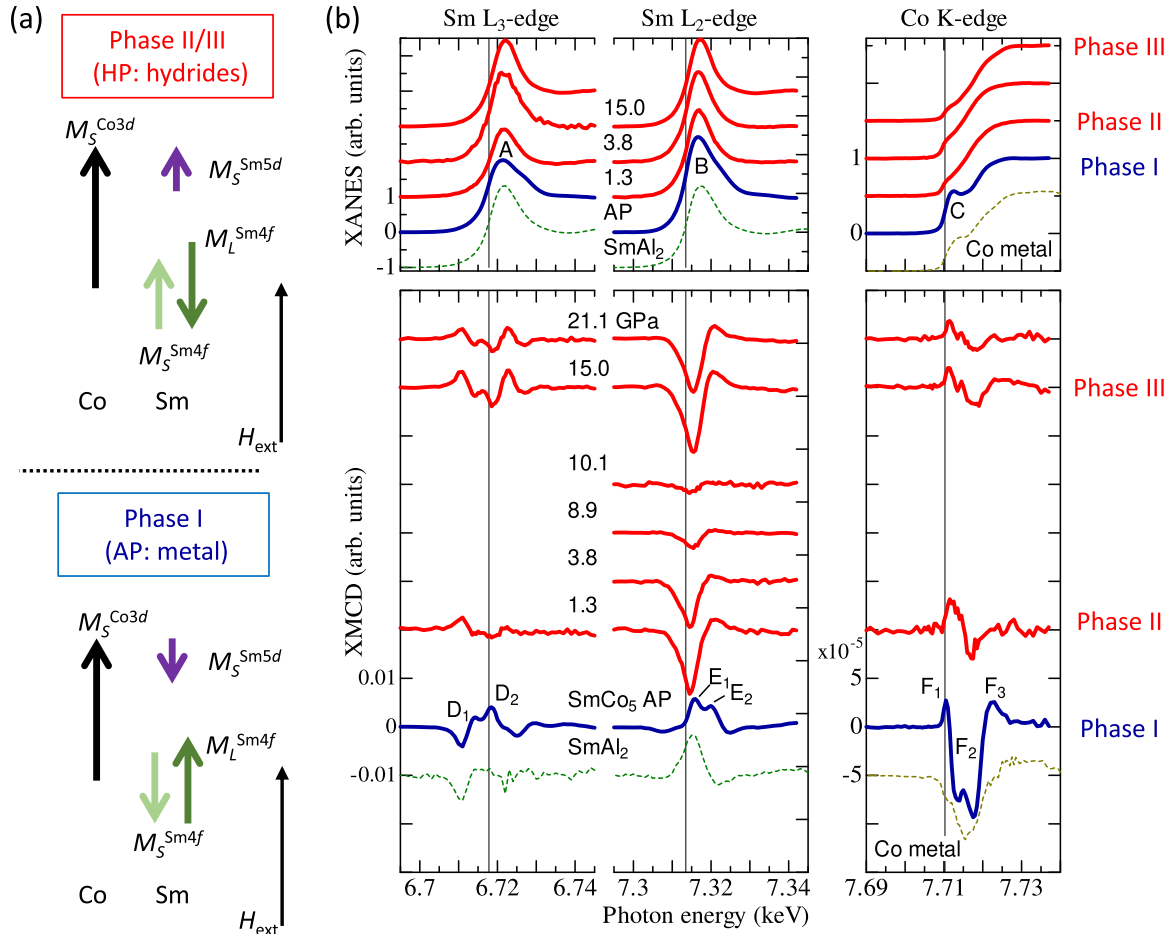


FIG. 1. (a) Initial (bottom) and hydrogenated (top) magnetic configurations of SmCo_5 . (b) XANES and XMCD spectra of SmCo_5H_x at $T = 15\text{--}16$ K and selected pressures together with the reference spectra of SmAl_2 and Co metal (dotted lines). The vertical lines indicate the absorption edge, E_0 . The characteristic profiles are labeled by A–F with subscripts.

Gd-doped SmCo_5 ($\text{Sm}_{0.92}\text{Gd}_{0.08}\text{Co}_5$). For this purpose, XMCD spectra at the Sm $L_{2,3}$ edges and Co K edge were measured. Moreover, the hydrogen content and crystal structure of SmCo_5H_x were determined by x-ray diffraction (XRD). First-principles calculations were also performed to discuss the hydrogen-induced electronic structures. The spin and orbital magnetic moments of the Sm^{3+} ground state were determined by Hund's rules as ${}^6H_{5/2}$, consequently, Sm^{3+} has a small total moment ($\sim 0.8\mu_B$ for a free ion, and comparable or larger moments for Sm atoms in metallic compounds), which is due to the slightly larger orbital moment than the spin moment coupled antiparallel [10–12]. SmCo_5 forms a hexagonal CaCu_5 -type structure (space group $P6/mmm$) and is a ferromagnetic permanent magnet consisting of $\sim 0.99(9)\mu_B$ for Sm at the $1a$ site, $\sim 2.22(8)\mu_B$ for Co at the $2c$ site, $\sim 2.24(8)\mu_B$ for Co at the $3g$ site, and all moments align parallel to the c axis [13]. Therefore, if the magnetic coupling reverses via the hydrogenation, it is very probable that the small moments of Sm flip to the direction opposite to the external magnetic field, H_{ext} , whereas the direction of larger Co moments remains unchanged. In this study, the expected change in the magnetic structure from the starting phase (phase I) to the hydrogenated phases (phases II and III) has been successfully observed, as illustrated in Fig. 1(a).

II. EXPERIMENTAL PROCEDURES

A commercially available ingot of nonmagnetized $\text{Sm}_{0.92}\text{Gd}_{0.08}\text{Co}_5$ was crashed into polycrystalline powder and pelletized for the XMCD and XRD measurements. The ingot contained a small portion of Gd to stabilize the magnetic properties as a permanent magnet, which allowed us to revisit the hydrogenation effects on heavy RE atoms. The 8 at.% content of Gd with respect to Sm was confirmed by the edge jump of the absorption profile at the Gd L_3 edge. The single phase of the CaCu_5 -type structure was confirmed for the samples by means of powder x-ray diffraction. The pelletized sample was loaded into the hole of a tungsten gasket together with H_2 fluid that was initially pressurized to 0.18–0.20 GPa. Versatile gas-loading systems available at SPring-8 [14] and the National Institute for Materials Science (NIMS) [15] were utilized for the H_2 fluid loading. The H_2 fluid functioned as a pressure-transmitting medium and the source of hydrogenation.

XMCD measurements were performed on the beamline BL39XU of SPring-8 [16]. Nanopolycrystalline diamonds were utilized for the anvils of diamond anvil cell (DAC) in order to avoid glitches superimposed on the x-ray absorption profile [17,18]. A diamond phase retarder was used to

generate right- and left-circularly polarized x rays. For the XMCD measurements, a magnetic field of $H_{\text{ext}} = 0.6$ T was applied parallel to the incident x ray. The incident x ray of BL39XU was focused to about $2.5(\text{v}) \times 8.0(\text{h}) \mu\text{m}^2$ in size using Kirkpatrick-Baez mirrors. XMCD spectra were measured at temperatures from ~ 15 to 300 K using a He-flow cryostat system with a clamp-type DAC. Because the pressure at the sample varied with cooling/heating by the thermal contraction of the DAC, the temperature-induced pressure variation at the sample was monitored at each P/T condition using an online ruby fluorescence measurement. A pressure calibration of quasihydrostatic pressure conditions was used [19].

XRD patterns were measured on BL10XU of Spring-8 at room temperature with x-ray wavelength of $\lambda = 0.413$ 10(7) Å [20]. Angular dispersive XRD patterns were recorded on the imaging plate at each pressure. During the exposure, the DAC was rotated several degrees around the vertical axis to improve the uniformity of the Debye-Scherrer rings. Two individual runs of the XRD measurements were performed.

The hydrogen effects on the spin polarization at Sm $5d$ states were investigated by first-principles calculation. The densities of state (DOS) of SmCo_5H_x were calculated using calculations based on density functional theory with the all-electron full-potential linear augmented plane wave (FLAPW) method using the WIEN2K package [21]. Exchange and correlation were treated within its spin-polarized form with the generalized gradient approximation (GGA) using Perdew-Burke-Ernzerhof (PBE) functions. Uniform k -mesh sets of $10 \times 10 \times 10$ were used for integration in the Brillouin zone. In our case, the augmented plane-wave plus local orbital (APW+lo) basis set was used, whereas the spin-orbit interaction was excluded. The muffin-tin sphere radii were set to 1.32 Å for Sm, 1.10 Å for Co, and 0.59 Å for H atoms.

III. RESULTS AND DISCUSSION

A. XANES and XMCD spectra

Figure 1(b) shows x-ray absorption near edge structure (XANES) and XMCD spectra of Co K and Sm L_2 and L_3 edges at selected pressures. The characteristic profiles are labeled as A–F with subscript numbers. XANES profiles at the Sm L_2 and L_3 edges are characterized by the white-line peaks near the absorption edge E_0 (labels A and B), which correspond to the transition of photoelectrons from Sm $2p$ to Sm $5d$ orbitals. The XANES profile at the Co K shows a shoulder structure near E_0 (label C), which is generated by the hybridization between Co $4p$ and Sm $5d$ orbitals. XMCD spectra of SmCo_5 show complicated profiles because XMCD spectra of RE-TM compounds contain multiple contributions from the electron orbitals of both RE and TM atoms [22–25]: XMCD spectra of Sm $L_{2,3}$ edges are composed of the profiles of the $2p \rightarrow 4f$ electric quadrupole (EQ) transition (D_1) and the Sm $2p \rightarrow 5d$ electric dipole (ED) transition (D_2 , E_1 , and E_2), where the Sm $5d$ orbital is spin polarized by the exchange interaction with the Sm $4f$ moment and hybridization with neighboring Co $3d$ states. In the case of XMCD at the Co K edge, the effect from the RE atom dominantly appears in the positive peaks (F_3) at $E = E_0 + 12$ eV, and both RE and TM contribute to the sharp positive peak (F_1) at $E = E_0$ [24],

indicating that the wide negative dip (F_2) located between the F_1 and F_3 peaks can be used to judge the direction of Co moment with respect to H_{ext} . The XMCD profiles of SmCo_5 revealed that both Sm and Co moments align parallel to H_{ext} before hydrogenation.

Hydrogenation altered XANES and XMCD spectra at all edges: The white-line peaks (labels A and B) of XANES become sharp and intense, and the shoulder structure labeled C disappears. XMCD at Sm L_2 exhibits a negative peak with a small positive hump at higher energies after hydrogenation, and the Sm L_3 edge XMCD completely reverses the sign of the profile. XMCD at the Co K edge modifies the profile significantly near E_0 . To distinguish the contribution of the Co $3d$ orbital from the others at the Sm $L_{2,3}$ edges, XMCD spectra of Laves phase SmAl_2 are displayed in Fig. 1(b) as a reference. Because Al atom is not magnetized, SmAl_2 provides XMCD spectra originating only from the exchange interaction between Sm $5d$ and Sm $4f$ orbitals. Therefore, the commonly observed peaks, D_1 , D_2 and E_1 , result from the magnetic polarization induced by the Sm $4f$ state. On the other hand, the profile labeled as E_2 is not observed in SmAl_2 , which corresponds to the profiles due to the Sm $5d$ –Co $3d$ hybridization.

The hybridization between electronic orbitals of Sm and Co atoms is weakened by hydrogenation, which results in the flipping of the Sm magnetic moment with respect to the direction of the Co magnetic moment and H_{ext} . The weakened hybridization is recognized by the disappearances of the shoulder C at the Co K edge and the peak E_2 at the Sm L_2 edge. The absence of peak E_2 leads to an XMCD profile composed of only the peak E_1 , which has a profile similar to that of SmAl_5 with a reversed sign. The opposite sign of the E_1 peak indicates that Sm $4f$ magnetic moment flips to the direction antiparallel to H_{ext} due to the hydrogenation. The completely reversed XMCD profile at the Sm L_3 edge also demonstrates that both Sm $5d$ and Sm $4f$ moments flip their direction, as illustrated in Fig. 1(a). Moreover, the positive sign of the EQ peak (label D_1) at the Sm L_3 XMCD gives direct evidence that Sm $4f$ moments align antiparallel to H_{ext} for SmCo_5H_x . We suppose that the ferrimagnetic relationship between spin and orbital components of Sm $4f$ electrons is conserved via Hund's third rule; therefore, each magnetic component flips due to the hydrogenation, as illustrated in Fig. 1(a).

We carefully determined the direction of the Co moment by comparing the XMCD profile with that of Co metal at the Co K edge. This is because XMCD of SmCo_5H_x at the Co K edge is attributed to the weakly polarized Co $4p$ orbital moments that are hybridized with Co $3d$ and Sm $5d$ orbitals of the neighboring atoms [26]. As shown in Fig. 1, the negative component of F_2 remains as a major component after hydrogenation, which preserves the sign similar to the XMCD of Co metal, even though F_1 and F_3 positive peaks increase and decrease, respectively. This result demonstrates that the Co moment is unchanged parallel to H_{ext} after hydrogenation. Because the Co moment is the major component in the net magnetization of SmCo_5 , the unchanged direction of the Co moment can reasonably stabilize the hydrogen-induced magnetic structure against the flipped Sm moment.

Two different magnetic phases (phases II and III) were found as hydrogenated phases by applying pressure to SmCo_5

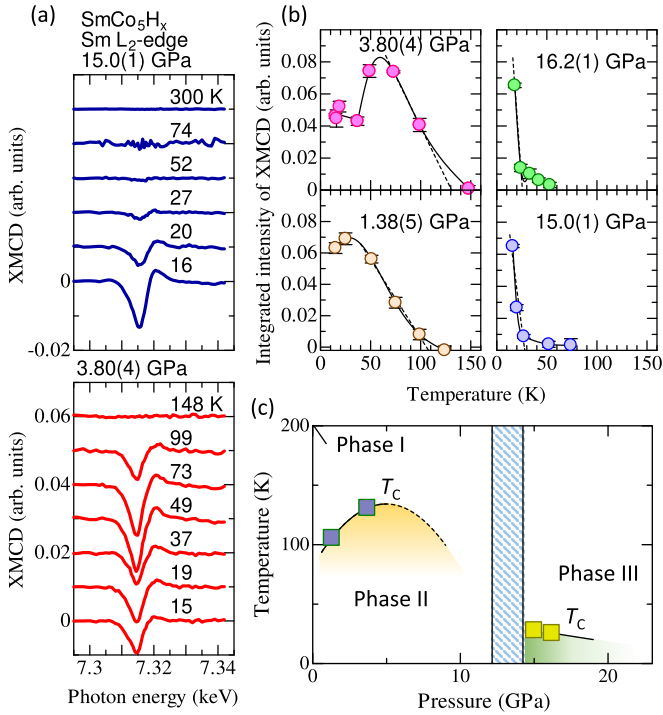


FIG. 2. (a) Temperature evolution of XMCD spectra at the Sm L_2 edge XMCD under 3.8 and 15.0 GPa. (b) Temperature dependences of integrated XMCD intensity under selected pressures. Solid and dashed lines are guides and fitted lines to estimate T_C , respectively. (c) P - T phase diagram of SmCo_5H_x .

(phase I). XMCD at Sm L_2 edge decreases gradually with increasing pressure, and shows the minimum intensity at 10.1 GPa, whereas it reappears at 15.0 GPa. Figures 2(a) and 2(b) display temperature dependence of Sm L_2 XMCD and the integrated XMCD of phases II and III at selected pressures. The XMCD intensity decreases rapidly with increasing temperature, and Curie temperatures T_C were determined to be 106, 131, 28, and 26 K, at 1.3, 3.8, 15.0, and 16.2 GPa, respectively, by linear extrapolation. Therefore, two ferrimagnetic phases, II and III, exist with flipping Sm moments at pressures below and above ~ 10.1 GPa, respectively. These phases are characterized by moderate and low T_C 's as summarized in the P - T phase diagram of Fig. 2(c). Compared with $T_C \sim 1300$ K of phase I [1], T_C 's of phase II and III were drastically low.

B. X-ray diffraction patterns

Different hydrogen-induced crystal structures were confirmed for phases II and III by x-ray diffraction patterns as shown in Fig. 3(a). Characteristic Bragg peaks of phases II and III are indicated by diamonds and stars, respectively. The structural parameters are summarized in Figs. 3(b)–3(f). The boundary between phases II and III appears as a coexistence region at approximately 13 GPa, which is represented by a hatched region in Figs. 3(b)–3(f). Crystal structures of phases II and III were determined and refined by software EXPO2014 [27] and GSAS-II [28], as shown in Fig. 3(g). The space group of phase II is similar to hexagonal $P6/mmm$ of phase I; however, the length of this phase is doubled in this phase of the c axis ($c_{\text{II}} \approx 2c_1$ with $a_{\text{II}} \approx a_1$). On the other hand, phase III

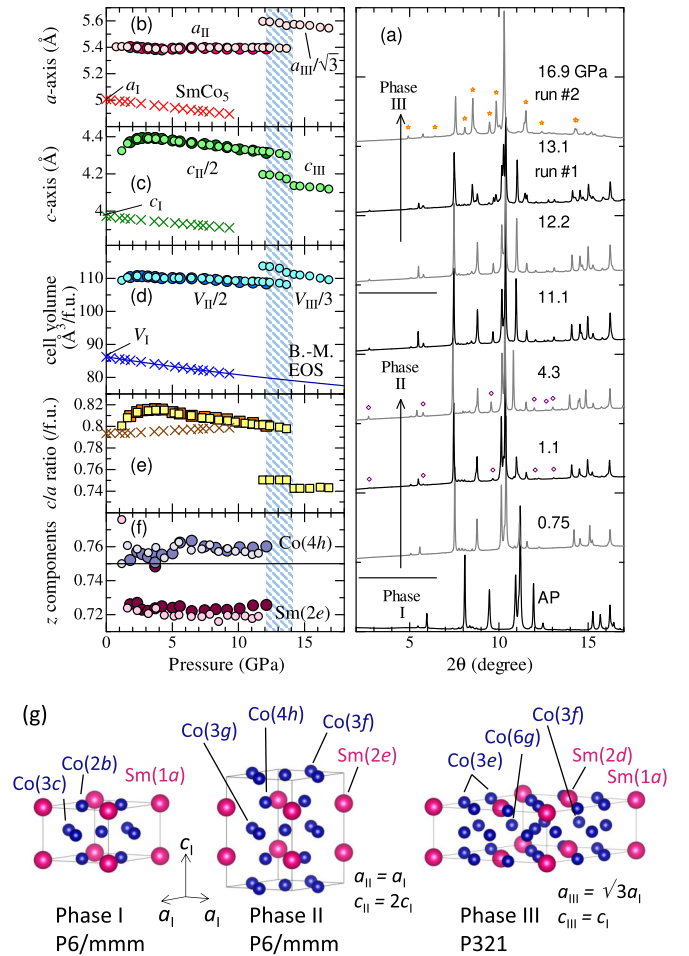


FIG. 3. (a) XRD patterns of SmCo_5H_x at selected pressures. Diamonds and stars indicate newly observed Bragg reflections for phases II and III, respectively. (b)–(f) Structural parameters determined by Rietveld refinements. Note that each structural parameter of phases II and III is converted to the parameter of phase I to highlight the structural changes. The hatched area corresponds to the coexistence region of phase II and III. The parameters of nonhydrogenated SmCo_5 are shown by cross marks for comparison. The solid line in panel (d) represents the fitted curves of the Birch-Murnaghan equations of state for the nonhydrogenated SmCo_5 . (g) Illustrations of the determined crystal structures of phases I, II, and III [30].

takes a longer a axis ($a_{\text{III}} \approx \sqrt{3}a_1$) and recovers the original c axis ($c_{\text{III}} \approx c_1$), leading to an approximately triple cell volume. The space group of phase III and the atomic positions were not explicitly determined, although trigonal $P321$ is a favorable space group that reproduces the experimental XRD pattern of phase III, as shown in Fig. S-1 of the Supplemental Material [29].

In Figs. 3(b)–3(e), the determined structural parameters were compared with the parameters of the nonhydrogenated SmCo_5 under normal compression using methanol:ethanol = 4:1 pressure medium. The structural parameters of SmCo_5 under high pressure are shown by cross marks for comparison. Each structural parameter of phases II and III is converted to the parameters of phase I to highlight the structural differences. Phase II allows displacements of Sm(2e) and Co(4h)

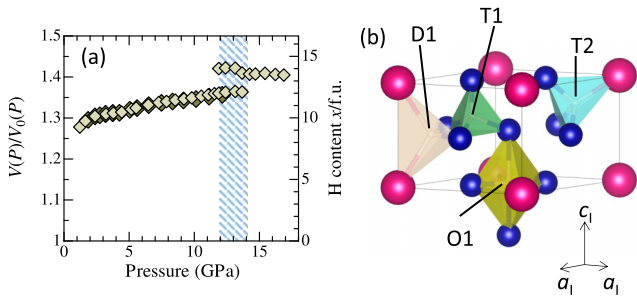


FIG. 4. (a) Volume expansion (left axis) and the corresponding hydrogen content x (right axis) of SmCo_5H_x as a function of pressure. The relationship between volume expansion and hydrogen content was determined by extrapolation from the reported relationships [32]. (b) Four kinds of polyhedrons, O1, D1, T1, and T2, in the SmCo_5 unit cell are shown as the hydrogen encapsulating structures. Their multiplicity in the cell is ignored, and the selected polyhedrons are shown.

atoms along the c axis; therefore, the atomic displacements in the double-sized cell generate new reflections as indicated by the diamond marks in Fig. 3(a). $\text{Sm}(2e)$ and $\text{Co}(4h)$ atoms are displaced to the opposite directions from the symmetric $z = 3/4$ position as summarized in 3(f). Elongation of lattice constant and subsequent volume expansions are observed via the hydrogenation to phases I \rightarrow II and II \rightarrow III, respectively. The c/a ratio of phases II and III represents anisotropic volume expansion that the c axis of phase II and a axis of phase III dominantly elongate due to the hydrogen occupation with increasing pressure.

C. Hydrogen contents and positions

The normalized volume expansion, which is defined as $[V(P) - V_0(P)]/V_0(P)$, was calculated to estimate the hydrogen content, x , quantitatively at each pressure P , where $V(P)$ and $V_0(P)$ are cell volumes of the hydride and non hydride compounds at a pressure P , respectively. The value of $V_0(P)$ was interpolated and extrapolated by a fit of the compression curve based on the second-order Birch-Murnaghan equation of state with a bulk modulus of 136(1) GPa. To the best of our knowledge, the relationship of x with the volume expansion has not been determined for SmCo_5H_x ; therefore, we recall the reported relationship for the cases of $\text{LaCo}_2\text{Ni}_3\text{H}_x$ [31] and RECo_5H_x (RE = La, Ce, Pr, and Nd) hydrides [32]. The result is shown in the Supplemental Material [29]. The volume expansion of RECo_5H_x traces a linear line as a function of x , which is independent of RE, whereas $\text{LaCo}_2\text{Ni}_3\text{H}_x$ also exhibits a linear trend but the slope is slightly smaller. Therefore, the hydrogen content x of SmCo_5H_x was evaluated using the extrapolation of the linear slope of RECo_5H_x . The linear trend of $\text{LaCo}_2\text{Ni}_3\text{H}_x$ was not utilized to avoid unexpected influences from Ni atoms. The relation $x(P) = (33.3 \pm 0.8) \times [V(P) - V_0(P)]/V_0(P)$, was used as summarized in Fig. 4(a). Consequently, a factor of 1.3 or larger volume expansion is converted to the dense hydrogen content, reaching to $x \sim 12$ (H/M ~ 2) for phase II and to $x \sim 13.5$ (H/M ~ 2.3) for phase III, where M = Sm + 5Co. The achieved hydrogen contents are much larger than the

known values for the AB_5 system, where hydrogenation up to $x = 5.6$ was the reported maximum value [31].

Hydrogen atoms occupy the inner space in four types of polyhedrons: Octahedral O1, dodecahedral D1, and tetragonal T1 and T2, as illustrated in Fig. 4(b). Three O1, four T1, and twelve T2 polyhedrons are contained in one SmCo_5 unit cell, and each polyhedron accommodates one H atom. Six D1 polyhedrons in the unit lattice form one dodecahedron that can accommodate two H atoms. According to theoretical calculations of LaCo_5H_x [33], the hydrogen occupations in the octahedral O1 and dodecahedral D1 are stable with a low enthalpy among the individual H occupation in the four polyhedrons. H atoms occupations in O1 and D1 sites up to $x = 5$ were experimentally observed under hydrogen pressures up to 1 MPa [32,34,35], whereas the occupation in the T2 polyhedrons should be introduced for the dense hydrogenation achieved in this study at more than 1 GPa. The occupation of multiple sites by hydrogen atoms, including the T2 sites, is theoretically allowed for dense hydrogenation: 2 + 8 H atoms in the D1 and T2 sites are predicted for $x = 10$ occupation subsequent to 2 + 2 H atoms in the O1 and D1 sites for $x = 4$ [33]. Hereafter, we use representations such as 2[D1]8[T2] and 2[O1]2[D1] to clarify the hydrogen content and the sites simultaneously. With increasing x from $x = 8$, a process of the hydrogen occupation is theoretically predicted: 8[T2] for $x = 8$, 2[D1]8[T2] for $x = 10$, 12[T2] for $x = 12$, 1[O1]12[T2] for $x = 13$, and 2[D1]12[T2] for $x = 14$. These models of hydrogen occupation are theoretically predicted as the energetically stable structures at each x . It is noted that the structure of $x = 8$ slightly deviates from the line connecting with the lowest energy structures [33]. The structural boundary between phases II and III is located at $x = 12$ to 13 as shown in Fig. 4.

Phases II and III exhibit anisotropic volume expansion to reduce the repulsion between M and H or H and H atoms. At pressures up to 3–4 GPa ($x \leq 10$), the c axis of phase II dominantly expands, which reduces the repulsion between M and H atoms in the T2 sites along the c axis. This hydrogenation displaces Co and Sm atoms along the c axis of phase II, as optimized by our Rietveld refinements. On the other hand, additional occupation of H atoms in T2 sites above 4 GPa ($10 \leq x \leq 12$) reduces the c/a ratio; therefore, expansion along the a axis becomes subsequently dominant for phase II, which suppresses the repulsive force working between H atoms in the same c plane. The minimum distance of 2.1 Å has been proposed as the empirical H-H distances under moderate pressure conditions [36]. Further hydrogenation above 12 GPa ($x \geq 12$) drastically expands the a axis, and consequently, the sample undergoes the structural change to phase III. This hypothesis is consistent with the theoretical models of Ref. [33], which state that hydrogen occupations at 1[O1] for $x = 13$ and 2[D1] for $x = 14$ are achieved together with 12[T2].

D. Hydrogen effects on the magnetic structures

To discuss the hydrogenation effect on the electronic and magnetic structures, first-principles calculations were performed. We used structural models up to $x = 12$ based on the theoretical prediction discussed above, where the

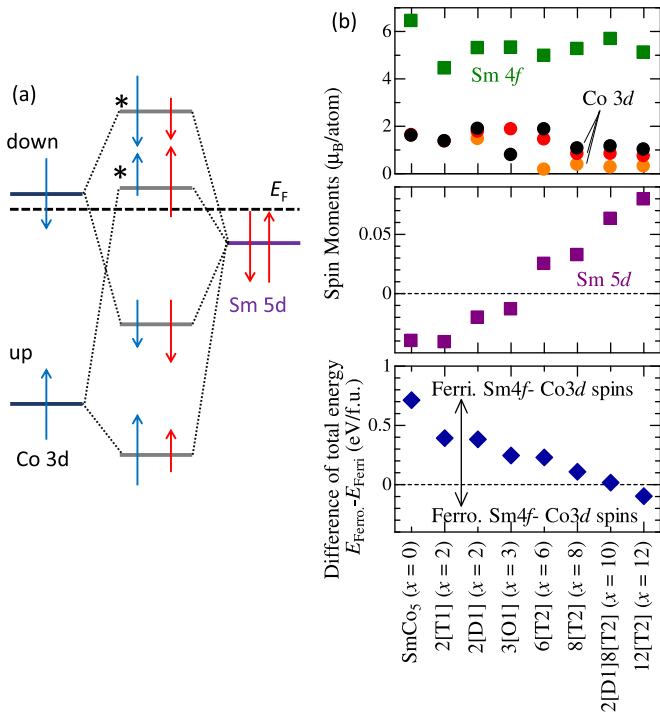


FIG. 5. (a) Schematic diagram of the magnetic interaction in SmCo_5 leading to the ferrimagnetic coupling of the $\text{Sm } 5d$ spin moment with $\text{Co } 3d$ spin moments. States with the asterisks correspond to antibonding states. (b) The top and middle panels show calculated spin magnetic moments of $\text{Sm } 5d$, $\text{Sm } 4f$, and $\text{Co } 3d$ states dependent on occupation of sites by H atoms in the case of the ferromagnetic coupling of $\text{Sm } 4f$ and $\text{Co } 3d$ spin moments. The bottom panel shows the total energy differences of the models between ferromagnetic and ferrimagnetic coupling of $\text{Sm } 4f$ and $\text{Co } 3d$ spin moments.

hydrogen atoms are partially and fully accommodated in the 12 T2 tetragonal sites. In our calculations, modification of the ferrimagnetic $\text{Sm } 5d$ – $\text{Co } 3d$ hybridization was focused to elucidate the drastic hydrogen effect on the magnetic coupling between Sm and Co, because both $\text{Sm } 4f$ – $\text{Sm } 5d$ ferromagnetic coupling and the spin-orbit coupling of $\text{Sm } 4f$ electrons are hardly influenced by the hydrogen occupation due to their intra-atomic nature of the interaction. As shown in Fig. 5(a), the energy diagram based on the molecular field theory demonstrates that the $\text{Sm } 5d$ – $\text{Co } 3d$ ferrimagnetic coupling is attributed to the large energy difference between up spin and down spin of $\text{Co } 3d$ states with respect to the small energy difference between up and down spins of $\text{Sm } 5d$ states located near the Fermi level [37]. Similar band structure was reproduced by our theoretical calculations of SmCo_5 . Therefore, we examined the weakening of the $\text{Sm } 5d$ – $\text{Co } 3d$ hybridization due to hydrogen occupation and changes in the magnetic coupling by the electronic structures up to $x = 12$ calculated using WIEN2K package [21]. Crystallographic configurations of H atoms occupation are summarized in Tables S-III and S-IV in the Supplemental Material [29]. Details of the calculation are also described there.

To simplify our model, only the $\text{Sm } 4f$ spin magnetic moment was calculated, and the calculation of the larger Sm

$4f$ orbital moments was excluded in our models. Two magnetic configurations of the ferrimagnetic and ferromagnetic $\text{Sm } 4f$ – $\text{Co } 3d$ spin couplings were examined, which correspond with the expected magnetic structures before and after hydrogenation, respectively. As shown in Fig. 5(b), the minus sign of the $\text{Sm } 5d$ moment and ferrimagnetic $\text{Sm } 5d$ – $\text{Co } 3d$ spin coupling remain unchanged for the models of 3[O1], 2[T1], and 2[D1] up to $x = 3$, which is independent to the types of the $\text{Sm } 4f$ – $\text{Co } 3d$ magnetic coupling, as shown in Fig. S-6 of the Supplemental Material [29]. In contrast, $x = 6$ or larger H atoms occupations at the T2 polyhedrons (models from 6[T2] to 12[T2]) flip the sign of the $\text{Sm } 5d$ spin moment to positive and realize the ferromagnetic $\text{Sm } 5d$ – $\text{Co } 3d$ spin coupling in the case of the ferromagnetic $\text{Sm } 4f$ – $\text{Co } 3d$ model. Although the flipping behavior of the $\text{Sm } 5d$ spin moment was not reproduced up to $x = 12$ in the model of the ferrimagnetic $\text{Sm } 4f$ – $\text{Co } 3d$ spin coupling, gradual suppression in the negative amplitude of the $\text{Sm } 5d$ spin component was observed as a similar trend of the hydrogenation. Therefore, the dense hydrogenation effect on the $\text{Sm } 5d$ state is successfully demonstrated for both cases. The magnetic coupling of ferromagnetic $\text{Sm } 5d$ – $\text{Co } 3d$ leads to a new spin configuration, where all spin moments of $\text{Co } 3d$, $\text{Sm } 5d$, and $\text{Sm } 4f$ states are oriented parallel to the H_{ext} . The larger $\text{Sm } 4f$ orbital moment should lie antiparallel to H_{ext} according to Hund’s third rule, leading to the ferrimagnetic configuration of SmCo_5H_x as illustrated in Fig. 1(a).

To confirm the stability of the ferromagnetic $\text{Sm } 4f$ – $\text{Co } 3d$ spin coupling by dense hydrogenation, we compared the total energy of this model with the model of ferrimagnetic $\text{Sm } 4f$ – $\text{Co } 3d$ spin coupling as a function of hydrogen content, x . The bottom panel of Fig. 5(b) shows a plot of the computed energy differences between two models. The plot demonstrates that hydrogenation of $0 \leq x \leq 8$, the ferrimagnetic $\text{Sm } 4f$ – $\text{Co } 3d$ spin coupling is stable, which is consistent with the magnetic structure based on SmCo_5 . On the other hand, the ferromagnetic $\text{Sm } 4f$ – $\text{Co } 3d$ spin coupling becomes energetically comparable at $x = 10$ and lower at $x = 12$. Therefore, our calculation is very consistent with our experimental results of the flipping of $\text{Sm } 4f$ moments at the estimated hydrogen content $x \geq 10$.

According to our calculations, the hydrogen occupation in T2 sites reduces the magnetic moment of the $\text{Co } 3d$ state, as shown in Fig. 5(b), which is probably due to the increasing hybridization of H with Sm/Co electronic orbitals. The suppressed magnetic polarization in the $\text{Co } 3d$ bands reconstructs the $\text{Sm } 5d$ – $\text{Co } 3d$ magnetic interaction from antiferromagnetic to ferromagnetic, as shown in the density of states displayed in Figs. S-4 and S-5 of the Supplemental Material [29]. We found that the dense hydrogenation introduces the unoccupied states in the up-spin band of $\text{Co } 3d$ near E_F , resulting in a change to weak ferromagnetism from the strong ferromagnetism, where strong and weak ferromagnetism are defined as $3d$ up-spin bands completely occupied and partially unoccupied, respectively. The H-induced modification of XMCD at the Co K edge (peaks F_1 and F_2) is a signature of the emergence of the weak ferromagnetism, which can be interpreted based on the discussion about the XMCD of iron and nickel [26]. The weak ferromagnetism reconstructs the energy balance between up spin and down spin of $\text{Co } 3d$

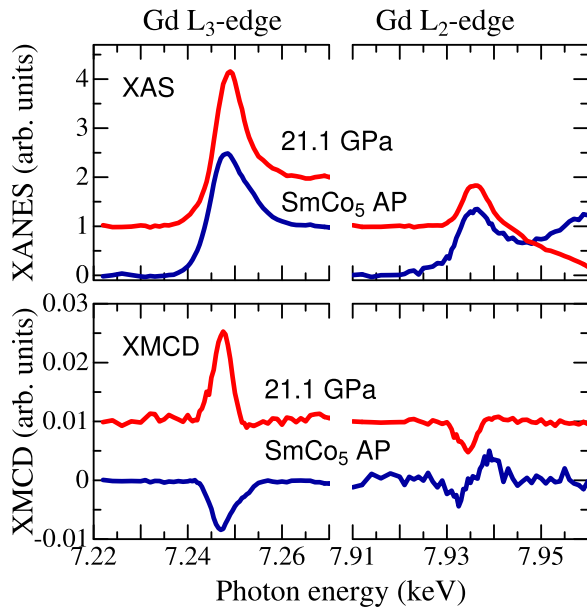


FIG. 6. XAS and XMCD spectra at the Gd $L_{2,3}$ edges of doped Gd atoms in $\text{Sm}_{0.92}\text{Gd}_{0.08}\text{Co}_5\text{H}_x$.

states with respect to the energy of Sm $5d$ states [Fig. 5(a)], consequently the ferrimagnetic coupling between Sm and Co moments arises after the dense hydrogenation.

E. Flipping of Gd moments

Interestingly, $4f$ magnetic moments of the doped Gd atoms also flipped together with the Sm $4f$ moment. Figure 6 shows that XMCD profiles of Gd reverse their sign after hydrogenation. Although the XMCD of SmCo_5 at the Gd L_2 edge is largely distorted by the strong negative component via the hybridization with the Co $3d$ state [38], flipping behavior was clearly observed at the Gd L_3 edge. The positive XMCD at the Gd L_3 edge and negative XMCD at the L_2 edge provide direct evidence that the Gd moment aligns parallel to H_{ext} at

21.1 GPa [39]; therefore, the magnetic coupling between Gd and Co moment changes from ferrimagnetic to ferromagnetic. Although the flipping of Gd and Sm moments occurs in opposite directions with respect to H_{ext} , the same mechanism is expected for the flipping processes.

IV. CONCLUDING REMARKS

This study demonstrates that dense hydrogenation of $\text{Sm}_{0.92}\text{Gd}_{0.08}\text{Co}_5\text{H}_x$ ranging up to $x = 13.5$ reverses ferromagnetic coupling between Sm and Co moments to ferrimagnetic coupling. On the other hand, the magnetic coupling between Gd and Co moment changes from ferrimagnetic to ferromagnetic. Therefore, the hydrogenation-induced flipping occurs for the magnetic coupling in RE-TM compounds not only with heavy rare-earth elements but also with light rare-earth elements. Two hydrogenated crystal structures were observed by x-ray powder diffraction. Our theoretical calculations indicated that hydrogen occupation in the T2 polyhedron plays a key role in the flipping of the magnetic coupling. The dense hydrogen occupation in the T2 site changes the direction of Sm $5d$ moments to align parallel to H_{ext} ; consequently, the magnetic couplings of Co $3d$ -Sm $5d$ and Co $3d$ -Sm $4f$ moments become ferromagnetic and ferrimagnetic, respectively. The moderate hydrogenation modifies only magnetic properties such as Curie temperature, magnetization, and magnetic anisotropy, whereas this study revealed that dense hydrogen occupation in the narrow space surrounded by RE and TM atoms is capable of flipping the magnetic coupling between RE and TM atoms. For further applications for a magnetic device, investigations to reduce pressures for the hydrogenation to T2 sites and surveys of new materials with low hydrogenation pressures are necessary.

ACKNOWLEDGMENTS

The x-ray absorption and diffraction measurements were performed at SPring-8 with the approval of PRC-JASRI (No. 2017A1289, No. 2018A1269, No. 2019A1530, No. 2019B1514, No. 2020A1540, No. 2020A1486, and No. 2021B1574).

- [1] *Rare-Earth Iron Permanent Magnets*, edited by J. M. D. Coey, Monographs on the Physics and Chemistry of Materials Vol. 54 (Clarendon, Oxford, 1996).
- [2] T. Jo and S. Imada, *J. Phys. Soc. Jpn.* **62**, 3721 (1993).
- [3] E. Gratz and A. S. Markosyan, *J. Phys.: Condens. Matter* **13**, R385 (2001).
- [4] R. Streubel, C.-H. Lambert, N. Kent, P. Ercius, A. T. N'Diaye, C. Ophus, S. Salahuddin, and P. Fischer, *Adv. Mater.* **30**, 1800199 (2018).
- [5] S. Mangin, M. Gottwald, C. Lambert, D. Steil, V. Uhlř, L. Pang, M. Hehn, S. Alebrand, M. Cinchetti, G. Malinowski, Y. Fainman, M. Aeschlimann, and E. E. Fullerton, *Nat. Mater.* **13**, 286 (2014).
- [6] N. Ishimatsu, H. Hashizume, S. Hamada, N. Hosoi, C. S. Nelson, C. T. Venkataraman, G. Srajer, and J. C. Lang, *Phys. Rev. B* **60**, 9596 (1999).
- [7] I. Bulyk, V. Chabanenko, A. Nabialek, T. Zajarniuk, A. Szewczyk, R. Puźniak, V. Burkhovetskyi, V. Tarenkov, J. Wrobel, and I. Borukh, *J. Alloys Compd.* **866**, 158272 (2021).
- [8] T. Mitsui, R. Masuda, M. Seto, N. Hirao, T. Matsuoka, Y. Nakamura, K. Sakaki, and H. Enoki, *J. Alloys Compd.* **580**, S264 (2013).
- [9] T. Mitsui, Y. Imai, N. Hirao, T. Matsuoka, Y. Nakamura, K. Sakaki, H. Enoki, N. Ishimatsu, R. Masuda, and M. Seto, *J. Phys. Soc. Jpn.* **85**, 123707 (2016).
- [10] E.-M. Anton, B. J. Ruck, C. Meyer, F. Natali, H. Warring, F. Wilhelm, A. Rogalev, V. N. Antonov, and H. J. Trodahl, *Phys. Rev. B* **87**, 134414 (2013).
- [11] M. Ungureanu, K. Dumesnil, C. Dufour, N. Gonzalez, F. Wilhelm, A. Smekhova, and A. Rogalev, *Phys. Rev. B* **82**, 174421 (2010).

- [12] S. Qiao, A. Kimura, H. Adachi, K. Iori, K. Miyamoto, T. Xie, H. Namatame, M. Taniguchi, A. Tanaka, T. Muro, S. Imada, and S. Suga, *Phys. Rev. B* **70**, 134418 (2004).
- [13] H. Kohlmann, T. C. Hansen, and V. Nassif, *Inorg. Chem.* **57**, 1702 (2018).
- [14] N. Hirao (unpublished).
- [15] K. Takemura, P. C. Sahu, Y. Kunii, and Y. Toma, *Rev. Sci. Instrum.* **72**, 3873 (2001).
- [16] N. Kawamura, N. Ishimatsu, and H. Maruyama, *J. Synchrotron Rad.* **16**, 730 (2009).
- [17] T. Irifune, A. Kurio, S. Sakamoto, T. Inoue, and H. Sumiya, *Nature (London)* **421**, 599 (2003).
- [18] N. Ishimatsu, K. Matsumoto, H. Maruyama, N. Kawamura, M. Mizumaki, H. Sumiya, and T. Irifune, *J. Synchrotron Rad.* **19**, 768 (2012).
- [19] H. K. Mao, J. Xu, and P. M. Bell, *J. Geophys. Res.: Solid Earth* **91**, 4673 (1986).
- [20] N. Hirao, S. I. Kawaguchi, K. Hirose, K. Shimizu, E. Ohtani, and Y. Ohishi, *Matter Rad. Extremes* **5**, 018403 (2020).
- [21] P. Blaha, K. Schwarz, G. Madsen, D. Kvasnicka, J. Luitz, R. Laskowski, F. Tran, and L. Marks, *WIEN2K: An Augmented Plane Wave Plus Local Orbitals Program for Calculating Crystal Properties* (Technische Universität Wien, Vienna, 2001).
- [22] K. Fukui, H. Ogasawara, A. Kotani, I. Harada, H. Maruyama, N. Kawamura, K. Kobayashi, J. Chaboy, and A. Marcelli, *Phys. Rev. B* **64**, 104405 (2001).
- [23] I. Harada, K. Asakura, A. Fujiwara, and A. Kotani, *J. Electron Spectros. Relat. Phenomena* **136**, 125 (2004), special issue, Progress in Core-Level Spectroscopy of Condensed Systems.
- [24] J. Chaboy, M. Á. Laguna-Marco, C. Piquer, R. Boada, H. Maruyama, and N. Kawamura, *J. Synchrotron Rad.* **15**, 440 (2008).
- [25] J. P. Rueff, R. M. Galéra, C. Giorgetti, E. Dartyge, C. Brouder, and M. Alouani, *Phys. Rev. B* **58**, 12271 (1998).
- [26] J.-i. Igarashi and K. Hirai, *Phys. Rev. B* **50**, 17820 (1994).
- [27] A. Altomare, C. Cuocci, C. Giacovazzo, A. Moliterni, R. Rizzi, N. Corriero, and A. Falcicchio, *J. Appl. Crystallogr.* **46**, 1231 (2013).
- [28] B. H. Toby and R. B. Von Dreele, *J. Appl. Crystallogr.* **46**, 544 (2013).
- [29] See Supplemental Material at <http://link.aps.org/supplemental/10.1103/PhysRevMaterials.7.024401> for details of structural refinements, hydrogen content and theoretical calculations.
- [30] K. Momma and F. Izumi, *J. Appl. Crystallogr.* **44**, 1272 (2011).
- [31] Y. Nakamura, T. Nomiyama, and E. Akiba, *J. Alloys Compd.* **413**, 54 (2006).
- [32] F. Kuijpers and B. loopstra, *J. Phys. Chem. Solids* **35**, 301 (1974).
- [33] J. F. Herbst and L. G. Hector, *Appl. Phys. Lett.* **85**, 3465 (2004).
- [34] Y. Nakamura, J. Nakamura, K. Iwase, and E. Akiba, *Nucl. Instrum. Methods Phys. Res., Sect. A* **600**, 297 (2009).
- [35] Y. Nakamura, R. C. Bowman, Jr., and E. Akiba, *J. Alloys Compd.* **431**, 148 (2007).
- [36] D. Westlake, *J. Less Common Metals* **90**, 251 (1983).
- [37] P. Mohn, *Magnetism in the Solid State: An Introduction*, Springer Series in Solid-State Sciences Vol. 134 (Springer, Berlin, 2006).
- [38] M. A. Laguna-Marco, J. Chaboy, and C. Piquer, *Phys. Rev. B* **77**, 125132 (2008).
- [39] E. Dartyge, F. Baudelet, C. Giorgetti, and S. Odin, *J. Alloys Compd.* **275-277**, 526 (1998).